



A multiscale model for eccentric and concentric cardiac growth through sarcomerogenesis

Serdar Göktepe^a, Oscar John Abilez^{b,c}, Kevin Kit Parker^d, Ellen Kuhl^{a,e,f,*}

^a Department of Mechanical Engineering, Stanford University, 496 Lomita Mall, Stanford, CA 94305, USA

^b Department of Bioengineering, Stanford University, 318 West Campus Drive, Stanford, CA 94305, USA

^c Department of Surgery, Stanford University, 318 West Campus Drive, Stanford, CA 94305, USA

^d Disease Biophysics Group, Harvard University, 29 Oxford Street, Cambridge, MA 02138, USA

^e Department of Bioengineering, Stanford University, 496 Lomita Mall, Stanford, CA 94305, USA

^f Department of Cardiothoracic Surgery, Stanford University, 496 Lomita Mall, Stanford, CA 94305, USA

ARTICLE INFO

Article history:

Received 6 March 2010

Received in revised form

4 April 2010

Accepted 23 April 2010

Available online 4 May 2010

Keywords:

Biomechanics

Growth

Finite element method

Hypertrophic cardiomyopathy

Sarcomerogenesis

ABSTRACT

We present a novel computational model for maladaptive cardiac growth in which kinematic changes of the cardiac chambers are attributed to alterations in cytoskeletal architecture and in cellular morphology. We adopt the concept of finite volume growth characterized through the multiplicative decomposition of the deformation gradient into an elastic part and a growth part. The functional form of its growth tensor is correlated to sarcomerogenesis, the creation and deposition of new sarcomere units. In response to chronic volume-overload, an increased diastolic wall strain leads to the addition of sarcomeres in series, resulting in a relative increase in cardiomyocyte length, associated with eccentric hypertrophy and ventricular dilation. In response to chronic pressure-overload, an increased systolic wall stress leads to the addition of sarcomeres in parallel, resulting in a relative increase in myocyte cross sectional area, associated with concentric hypertrophy and ventricular wall thickening. The continuum equations for both forms of maladaptive growth are discretized in space using a nonlinear finite element approach, and discretized in time using the implicit Euler backward scheme. We explore a generic bi-ventricular heart model in response to volume- and pressure-overload to demonstrate how local changes in cellular morphology translate into global alterations in cardiac form and function.

© 2010 Elsevier Ltd. All rights reserved.

1. Motivation

Cardiovascular disease is the leading cause of death and disability in both industrialized nations and the developing world, accounting for approximately 40% of all human mortality (Rosamond et al., 2007). Despite tremendous scientific progress during the past 20 years, heart failure remains one of the most common, costly, disabling, and deadly medical conditions affecting more than 25 million people worldwide (Libby et al., 2007). Unlike many types of tissue in the body, diseased cardiac tissue does not regenerate and its damage is usually fatal (Emmanouilides et al., 1994). In hypertrophic cardiomyopathy, mechanical stimuli in the form of volume- and pressure-overload are believed

to be the major driving forces for disease initiation and disease progression (Kumar et al., 2005). On the cellular level, cardiac hypertrophy is initiated by alterations in cytoskeletal architecture and in cellular morphology. On the organ level, these changes manifest themselves in ventricular dilation or wall thickening (Berne and Levy, 2001; Opie, 2003). In an attempt to better understand the pathology of maladaptive cardiac growth, we seek to answer two fundamental questions: *How do local changes in cellular morphology and cytoskeletal architecture translate into global alterations in cardiac form and function?* and *How are these changes regulated by mechanical factors?*

The functional contractile unit of a cardiac cell is the sarcomere, a 1.9–2.1 μm long parallel arrangement of thick filaments of myosin that slide along thin filaments of actin (Bray et al., 2008; Mansour et al., 2004). Approximately 50 sarcomeres in series make up a myofibril; about 50–100 myofibrils in parallel make up a cardiomyocyte (Sanger et al., 2000). Healthy cardiomyocytes have a cylindrical shape with a length of approximately 100 μm and a diameter of 10–25 μm, consisting of a total of about 5000 sarcomere units (Opie, 2003). Fig. 1 displays an adult ventricular cardiomyocyte with the sarcomeric actin labeled in

* Corresponding author at: Department of Mechanical Engineering, Stanford University, 496 Lomita Mall, Stanford, CA 94305, USA. Tel.: +1 650 450 0855; fax: +1 650 725 1587.

E-mail addresses: goktepe@stanford.edu (S. Göktepe), ojabilez@stanford.edu (O.J. Abilez), kkparker@seas.harvard.edu (K.K. Parker), ekuhl@stanford.edu (E. Kuhl).

URL: <http://biomechanics.stanford.edu> (E. Kuhl).

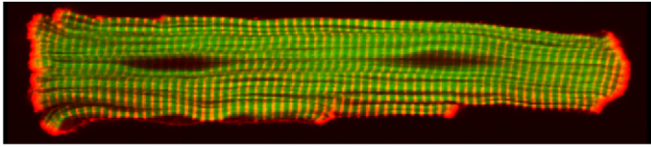


Fig. 1. Adult ventricular cardiomyocyte. The sarcomeric actin is labeled in green and the periodically spaced t-tubule system is marked in red, giving the cell its characteristic striated appearance. Healthy cardiomyocytes have a cylindrical shape with a diameter of 10–25 μm and a length of $\sim 100 \mu\text{m}$, consisting of approximately 50 sarcomere units in series making up a myofibril and 50–100 myofibrils in parallel. Cardiac disease can be attributed to structural changes in the cardiomyocyte, either through eccentric growth in dilated cardiomyopathy or through concentric growth in hypertrophic cardiomyopathy. (For interpretation of the references to color in this figure legend, the reader is referred to the web version of this article.)

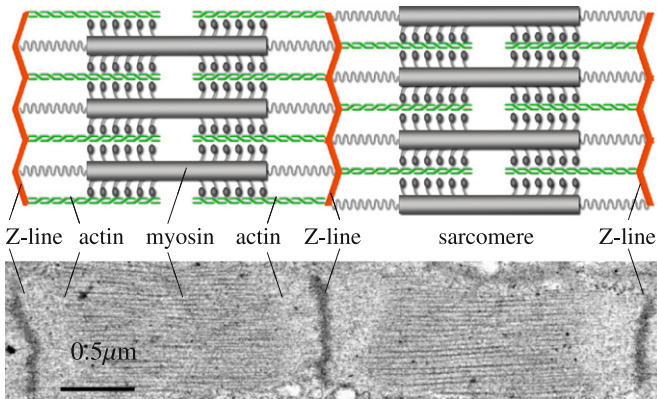


Fig. 2. Sarcomere units of human embryonic stem cell-derived cardiomyocyte. Sarcomeres are defined as the segment between two neighboring Z-lines, shown in red, which appear as dark lines under the transmission electron microscope. Healthy sarcomeres are 1.9–2.1 μm long characterized through a parallel arrangement of thick filaments of myosin, displayed in grey, sliding along thin filaments of actin, labeled in green. Although cardiac cells are known to change length and thickness in response to mechanical loading, the individual sarcomeres maintain an optimal resting length. (For interpretation of the references to color in this figure legend, the reader is referred to the web version of this article.)

green. Each cardiomyocyte is bounded by an external membrane called the sarcolemma, which invaginates perpendicular to the long axis of the cell to form an extensive tubular network. In Fig. 1, this periodically spaced T-tubule system is stained in red (Geisse et al., 2009). Fig. 2 illustrates individual sarcomere units as the segments between two neighboring Z-lines. In the transmission electron microscope image of a human embryonic stem cell-derived cardiomyocyte shown below, the Z-lines appear as dark lines giving the cell its characteristic striated appearance.

Historically, it has been believed that the contribution of cardiomyocytes to cardiac remodeling is primarily due to hypertrophy rather than hyperplasia, i.e., that cardiomyocytes are able to grow in size but not in number. They do so through sarcomerogenesis, the creation and deposition of new sarcomere units (Emmanouilides et al., 1994; Kumar et al., 2005). A commonly accepted measure to characterize cardiomyocyte morphology is their length-to-width ratio which is approximately 7:1 in the healthy mammalian myocardium (Gerdes, 2002). Cardiomyocyte morphology exhibits distinct variation in various pathological conditions (Gerdes and Capasso, 1995; Taber, 1995). In response to chronic volume-overload, elevated diastolic wall strains initiate the addition of sarcomeres in series, which manifest themselves in a relative increase in cardiomyocyte length without a significant change of cross sectional area. Accordingly, the length-to-width ratio may increase to approxi-

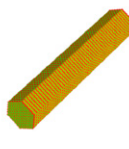
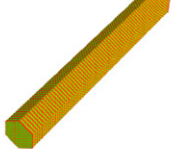
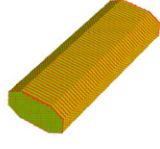
healthy cardiomyocyte	eccentric hypertrophy	concentric hypertrophy
		
physiological loading	volume overload	pressure overload
$\lambda^e \leq \lambda^{\text{crit}}, p \leq p^{\text{crit}}$	$\lambda^e > \lambda^{\text{crit}}$	$p > p^{\text{crit}}$
healthy heart	ventricular dilation	wall thickening
		

Fig. 3. Eccentric and concentric growth on the cellular and organ levels. Compared with the normal heart (left), volume-overload induced eccentric hypertrophy is associated with cell lengthening through the serial deposition of sarcomere units and manifests itself in ventricular dilation in response to volume-overload (center). Pressure-overload induced concentric hypertrophy is associated with cell thickening through the parallel deposition of sarcomere units and manifests itself in ventricular wall thickening in response to pressure-overload (right).

mately 11:1 (Gerdes et al., 1992). This type of cardiac growth, which is associated with ventricular dilation on the macroscopic level, is referred to as eccentric hypertrophy. In response to chronic pressure-overload, however, elevated systolic wall stresses initiate the addition of sarcomeres in parallel, which manifest themselves in a relative increase in myocyte cross sectional area without significant changes in cell length. Accordingly, the length-to-width ratio may decrease to approximately 3:1 (McCrosan et al., 2004; Sawada and Kawamura, 1991). This type of cardiac growth, which is associated with ventricular wall thickening on the macroscopic level, is referred to as concentric hypertrophy. The mechanical characteristics of these two forms of maladaptive cardiac growth are summarized in Fig. 3. They are known to initiate significant changes in phenotype, secondary to the reactivation of portfolios of genes that are normally expressed post-natally and that are correlated with contractile dysfunction (Hunter and Chien, 1999).

In this manuscript, we develop a novel continuum model and a computational simulation tool to predict eccentric and concentric growth as natural consequences of the strain-driven serial alignment and the stress-driven parallel bundling of newly generated sarcomeres units. *Our key kinematic assumption is that the individual cardiomyocytes deform affinely with the surrounding myocardial tissue.* Even though cardiomyocytes comprise only one-fourth of the total number of cells in the heart, this approach seems justified since they account for more than 90% of the total cardiac muscle volume (Kumar et al., 2005). Accordingly, we attribute pathological changes in cardiac volume exclusively to morphological changes of the cardiomyocytes themselves and neglect extracellular matrix remodeling (Himpel et al., 2008; Kuhl et al., 2005; Kuhl and Holzapfel, 2007). It has been demonstrated experimentally that remodeling and myocyte slippage play a rather insignificant role during cardiac growth (Gerdes et al., 1992). Accordingly, we adopt the framework of volumetric growth characterized through the concept of an incompatible

growth configuration (Rodriguez et al., 1994), which was originally developed in the context of finite strain plasticity (Lee, 1969). Continuum theories of finite growth have been studied intensely within the last decade (Epstein and Maugin, 2000; Goriely and Ben Amar, 2007; Lubarda and Hoger, 2002; Verdier et al., 2009), and the essential findings have been summarized comprehensively in a recent monograph (Ambrosi et al., 2009). Continuum growth theories have been applied successfully to characterize growing cell membranes (Goriely and Tabor, 2003), tumors (Ambrosi and Mollica, 2002), vascular tissue (Kuhl et al., 2007; Taber and Humphrey, 2001; Zohdi et al., 2004), and cardiac tissue (Göktepe et al., 2010c; Kroon et al., 2009). While earlier studies are primarily of theoretical and analytical nature (Garikipati, 2009; Humphrey, 2002; Taber, 1995), we can now observe a clear trend towards the computational modeling of volumetric growth (Alford and Taber, 2008; Himpel et al., 2005; Kroon et al., 2009; Menzel, 2005). By closely correlating macroscopic tissue growth to microscopic observations on the cellular level (Cox, 2010), we inherently resolve two of the major shortcomings of the phenomenological theory of volumetric growth: the appropriate characterization of the growth tensor and the definition of constitutive equations for its temporal evolution.

This manuscript is organized as follows. In Section 2, we outline the generic framework of volumetric growth, and specify the governing equations to characterize eccentric and concentric growth. We discuss the continuous equations, their temporal discretization, and their consistent linearization. In Section 3, we first summarize our generic bi-ventricular heart model with its loading and boundary conditions. Next, we subject this prototype model to eccentric and concentric growth to explore how changes in local cardiomyocyte morphology translate into alterations in cardiac form and function. We conclude with a final discussion in Section 4.

2. Methods

In this section, we first illustrate the governing equations for volumetric growth. We then specify the generic set of equations to strain-driven eccentric growth and to stress-driven concentric growth. For both, we outline the continuum framework and its algorithmic counterpart, including the temporal discretization and the consistent linearization of the local and global residual equations.

2.1. Generic framework of volumetric growth

We begin by briefly summarizing the governing equations of volumetric growth within a geometrically nonlinear setting. To characterize growth, we adopt the multiplicative decomposition of deformation gradient \mathbf{F} into an elastic part \mathbf{F}^e and a growth part \mathbf{F}^g (Rodriguez et al., 1994),

$$\mathbf{F} = \mathbf{F}^e \cdot \mathbf{F}^g \quad \text{with} \quad \mathbf{F} = \nabla_{\mathbf{x}} \phi \quad (1)$$

a concept that was first proposed in the context of finite elastoplasticity (Lee, 1969). This allows us to introduce the right Cauchy Green tensor \mathbf{C} and its elastic counterpart \mathbf{C}^e ,

$$\mathbf{C} = \mathbf{F}^t \cdot \mathbf{F}, \quad \mathbf{C}^e = \mathbf{F}^{et} \cdot \mathbf{F}^e = \mathbf{F}^{g-t} \cdot \mathbf{C} \cdot \mathbf{F}^{g-1} \quad (2)$$

whereby the latter can be interpreted as the covariant push forward of \mathbf{C} to the incompatible growth configuration. In the absence of transient terms and external forces, the balance of linear momentum can be expressed in the following reduced format:

$$\text{Div}(\mathbf{P}) = \mathbf{0} \quad \text{with} \quad \mathbf{P} = \mathbf{F} \cdot \mathbf{S} \quad (3)$$

where $\text{Div}(\cdot)$ denotes the derivative with respect to the material position \mathbf{X} , \mathbf{P} denotes the Piola stress, and \mathbf{S} denotes the second Piola Kirchhoff stress, respectively. A thermodynamically consistent stress definition can be derived from the dissipation inequality,

$$\mathcal{D} = \mathbf{S} : \frac{1}{2} \dot{\mathbf{C}} - \dot{\psi} \geq 0 \quad (4)$$

which we state here in its closed system format for the sake of transparency. For discussions on advanced versions of the dissipation inequality in the context of open system thermodynamics we refer to the related literature (Epstein and Maugin, 2000; Himpel et al., 2005; Kuhl and Steinmann, 2003a, 2003b; Lubarda and Hoger, 2002). For the sake of transparency, let us assume an isotropic elastic response that can be characterized exclusively in terms of the right Cauchy Green tensor of the intermediate configuration $\mathbf{C}^e = \mathbf{F}^{g-t} \cdot \mathbf{C} \cdot \mathbf{F}^{g-1}$. Following standard arguments of thermodynamics, we can then introduce the Helmholtz free energy as $\psi = \psi(\mathbf{F}^e)$, or reparameterize it conveniently in terms of the total deformation gradient \mathbf{F} and the set of internal variables \mathbf{F}^g as $\psi = \psi(\mathbf{F}, \mathbf{F}^g)$, and evaluate the dissipation inequality (4):

$$\mathcal{D} = \left[\mathbf{S} - 2 \frac{\partial \psi}{\partial \mathbf{C}} \right] : \frac{1}{2} \dot{\mathbf{C}} + \mathbf{M}^e : \mathbf{L}^g \geq 0 \quad (5)$$

Herein, $\mathbf{M}^e = \mathbf{C}^e \cdot \mathbf{S}^e$ denotes the Mandel stress (Epstein and Maugin, 2000), which is thermodynamically conjugate to the growth velocity gradient $\mathbf{L}^g = \dot{\mathbf{F}}^g \cdot \mathbf{F}^{g-1}$. We immediately obtain the definition for the second Piola–Kirchhoff stress \mathbf{S} as thermodynamically conjugate quantity to the right Cauchy Green deformation tensor \mathbf{C} ,

$$\mathbf{S} = 2 \frac{\partial \psi}{\partial \mathbf{C}} = \mathbf{F}^{g-1} \cdot \mathbf{S}^e \cdot \mathbf{F}^{g-t} \quad \text{with} \quad \mathbf{S}^e := 2 \frac{\partial \psi}{\partial \mathbf{C}^e} \quad (6)$$

where \mathbf{S} takes the interpretation of the contravariant pull back of the intermediate second Piola Kirchhoff stress \mathbf{S}^e to the undeformed reference configuration. Just as a side remark, the elastic constitutive moduli \mathbf{L}^e related to the intermediate configuration can be obtained by taking the second derivative of the Helmholtz free energy ψ with respect to the corresponding kinematic quantity \mathbf{C}^e .

$$\mathbf{L}^e = 2 \frac{\partial \mathbf{S}^e}{\partial \mathbf{C}^e} = 4 \frac{\partial^2 \psi}{\partial \mathbf{C}^e \otimes \partial \mathbf{C}^e} \quad (7)$$

It remains to define the growth tensor \mathbf{F}^g , for which we adopt the common assumption of symmetry, i.e., $\mathbf{F}^g = \mathbf{F}^{g-t}$. As a natural consequence, the entire rotation is lumped into the elastic part of the deformation gradient \mathbf{F}^e , and the plastic spin in the fictitious intermediate configuration vanishes identically (Boyce and Weber, 1989; Naghdi, 1990). Taking into account the orthotropic nature of most biological tissue, we introduce the growth tensor in the following generic format:

$$\mathbf{F}^g = \mathcal{J}^f \mathbf{f}_0 \otimes \mathbf{f}_0 + \mathcal{J}^s \mathbf{s}_0 \otimes \mathbf{s}_0 + \mathcal{J}^n \mathbf{n}_0 \otimes \mathbf{n}_0 \quad (8)$$

where $\mathbf{f}_0, \mathbf{s}_0$ and \mathbf{n}_0 are the unit vectors of the orthotropic microstructure in the reference configuration and $\mathcal{J}^g = [\mathcal{J}^f, \mathcal{J}^s, \mathcal{J}^n]$ denotes the set of internal variables which are often referred to as growth multipliers. These take the value one in the plain elastic case, are smaller than one for shrinkage, and larger than one for growth. To complete the set of constitutive equations, we need to specify the evolution of the internal variables $\dot{\mathcal{J}}^g$:

$$\dot{\mathcal{J}}^g = \mathbf{k}^g(\mathcal{J}^g) \cdot \varphi^g(\mathbf{F}^e) \quad \text{or} \quad \dot{\mathcal{J}}^g = \mathbf{k}^g(\mathcal{J}^g) \cdot \varphi^g(\mathbf{M}^e) \quad (9)$$

A common format is to introduce mechanically driven growth criteria ϕ^g which are only activated if a mechanical driving force exceeds a certain physiological threshold level. They can either be strain-driven, $\phi^g(\mathbf{F}^e)$, in analogy to finite strain damage, or stress-driven, $\phi^g(\mathbf{M}^e)$, in analogy to finite strain plasticity. In addition, the growth criteria are typically weighted by a matrix of growth

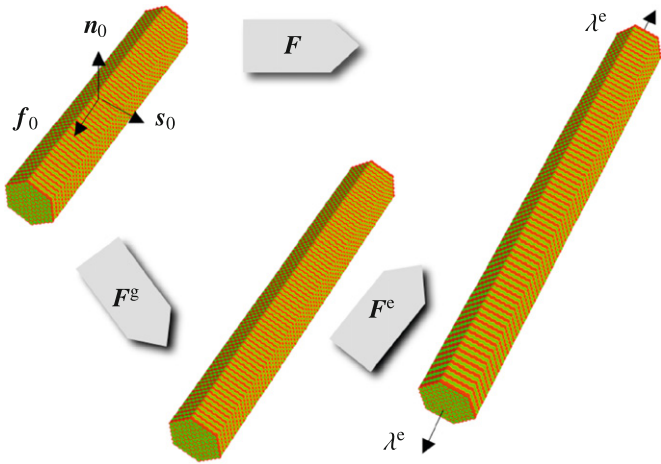


Fig. 4. Kinematics of eccentric growth. Serial sarcomeres deposition induces eccentric cardiomyocyte growth $\mathbf{F}^g = \mathbf{I} + [\vartheta^g - 1]\mathbf{f}_0 \otimes \mathbf{f}_0$ associated with cardiomyocyte lengthening along the \mathbf{f}_0 -axis, i.e., along the axis of cardiomyocyte stretch. Sarcomere deposition is driven by a strain-driven growth criterion $\phi^g = \lambda^e - \lambda^{\text{crit}}$, which is activated if the elastic stretch λ^e exceeds a critical physiological stretch level λ^{crit} . In the above example for $\vartheta^g = 1.4$, \mathbf{F}^g characterizes the serial deposition of 20 sarcomere units in length inducing a cell lengthening from 50 sarcomeres at 100 μm to 70 sarcomeres at 140 μm . \mathbf{F}^e reflects a cell stretch at a constant number of sarcomere units, with the individual sarcomeres undergoing an elastic stretch λ^e .

functions $\mathbf{k}^g(\vartheta^g)$ to ensure that the material does not grow unboundedly. For the special case of scalar-valued growth, ϑ^g , k^g , and ϕ^g are of course scalars as well. Constitutive assumptions for particular growth tensors (8) and evolution equation (9) for strain-driven eccentric growth and stress-driven concentric growth will be specified in Sections 2.2 and 2.3.

2.2. Strain-driven eccentric growth

In this section, we specify the generic set of equations to characterize pathophysiological eccentric cardiomyocyte growth, which we represent as a strain-driven, transversely isotropic, irreversible process. Eccentric growth is characterized through one single growth multiplier $\vartheta^g = \vartheta^f$ that reflects serial sarcomere deposition and induces an irreversible cardiomyocyte lengthening along the cell's long axis \mathbf{f}_0 , while there is no growth in the transverse direction $\vartheta^s = \vartheta^n = 1$, see Fig. 4. The generic growth tensor \mathbf{F}^g introduced in Eq. (8) can thus be expressed exclusively in terms of the eccentric growth multiplier ϑ^g .

$$\mathbf{F}^g = \mathbf{I} + [\vartheta^g - 1]\mathbf{f}_0 \otimes \mathbf{f}_0 \quad (10)$$

Motivated by physiological observations of volume-overload induced cardiac dilation, we introduce a strain-driven evolution law for the eccentric growth multiplier ϑ^g :

$$\dot{\vartheta}^g = k^g(\vartheta^g)\phi^g(\lambda^e) \quad (11)$$

It is based on an eccentric growth criterion ϕ^g weighted by a function k^g :

$$k^g = \frac{1}{\tau} \left[\frac{\vartheta^{\text{max}} - \vartheta^g}{\vartheta^{\text{max}} - 1} \right]^\gamma \quad \text{with} \quad \frac{\partial k^g}{\partial \vartheta^g} = -\frac{\gamma}{[\vartheta^{\text{max}} - \vartheta^g]} k^g \quad (12)$$

which is parameterized in terms of the sarcomere deposition time τ , the sarcomere deposition nonlinearity γ , and the maximum pathological cardiomyocyte stretch ϑ^{max} . For example, a maximum serial sarcomere deposition of $\vartheta^{\text{max}} = 1.4$ would allow for a possible deposition of 20 sarcomeres in length

resulting in a total cardiomyocyte length of 70 sarcomeres. This would correspond to a cell lengthening from 100 to 140 μm , see Fig. 4. The eccentric growth criterion ϕ^g is expressed in terms of the elastic overstretch $\lambda^e - \lambda^{\text{crit}}$,

$$\phi^g = \lambda^e - \lambda^{\text{crit}} = \frac{1}{\vartheta^g} \lambda - \lambda^{\text{crit}} \quad \text{with} \quad \frac{\partial \phi^g}{\partial \vartheta^g} = -\frac{1}{\vartheta^g{}^2} \lambda \quad (13)$$

such that growth is activated only if the elastic stretch λ^e exceeds a critical physiological threshold value λ^{crit} . Note that the derivatives in Eqs. (12.2) and (13.2) will later become essential for the consistent algorithmic linearization within an incremental iterative Newton Raphson scheme. In cardiac dilation, growth is actually one dimensional, and the total cardiomyocyte stretch $\lambda = [\mathbf{f}_0 \cdot \mathbf{F}^t \cdot \mathbf{F} \cdot \mathbf{f}_0]^{1/2} = \lambda^e \lambda^g$ along the long axis \mathbf{f}_0 obeys a multiplicative decomposition similar to the deformation gradient itself. It can thus be expressed as the product of the elastic stretch λ^e , i.e., the healthy cardiomyocyte stretch during diastole, and the growth stretch $\lambda^g = \vartheta^g$, i.e., the pathological cardiomyocyte stretch during eccentric growth. Our goal is to solve the evolution equation (11) to determine the current growth multiplier ϑ^g for a given current deformation state \mathbf{F} at the current time t , assuming we know the growth multiplier ϑ_n^g at the end of the previous time step t_n . We introduce the following finite difference approximation of the first order material time derivative,

$$\dot{\vartheta}^g = [\vartheta^g - \vartheta_n^g] / \Delta t \quad (14)$$

where $\Delta t := t - t_n > 0$ denotes the actual time increment. In the spirit of implicit Euler backward type time stepping schemes, we now reformulate the evolution equation (11) with the help of the finite difference approximation (14) introducing the discrete residual \mathbf{R}^g in terms of the unknown growth multiplier ϑ^g :

$$\mathbf{R}^g = \vartheta^g - \vartheta_n^g - \frac{1}{\tau} \left[\frac{\vartheta^{\text{max}} - \vartheta^g}{\vartheta^{\text{max}} - 1} \right]^\gamma \left[\frac{1}{\vartheta^g} \lambda - \lambda^{\text{crit}} \right] \Delta t \approx 0 \quad (15)$$

Its linearization renders the tangent for local Newton iteration,

$$\mathbf{K}^g = \frac{d\mathbf{R}^g}{d\vartheta^g} = 1 - \left[k^g \frac{\partial \phi^g}{\partial \vartheta^g} + \phi^g \frac{\partial k^g}{\partial \vartheta^g} \right] \Delta t \quad (16)$$

in terms of the expressions given in (12) and (13). The local residual and the local tangent define the iterative update of the eccentric growth multiplier $\vartheta^g \leftarrow \vartheta^g - \mathbf{R}^g / \mathbf{K}^g$. Once we have determined the growth multiplier ϑ^g , we can update the growth tensor $\mathbf{F}^g = \mathbf{I} + [\vartheta^g - 1]\mathbf{f}_0 \otimes \mathbf{f}_0$ from Eq. (10), the elastic tensor $\mathbf{F}^e = \mathbf{F} \cdot \mathbf{F}^{g-1}$ from Eq. (1), the elastic stress $\mathbf{S}^e = 2\partial\psi/\partial\mathbf{C}^e$ from Eq. (6), and lastly, the second Piola Kirchhoff stress \mathbf{S} from Eq. (6):

$$\mathbf{S} = \mathbf{F}^{g-1} \cdot \mathbf{S}^e \cdot \mathbf{F}^{g-t} \quad \text{with} \quad \mathbf{S}^e = 2 \frac{\partial \psi}{\partial \mathbf{C}^e} \quad (17)$$

This second Piola Kirchhoff stress enters the equilibrium equation (3), or, in the notion of the finite element method, the expression for the global discrete residual. Its linearization with respect to the total right Cauchy Green tensor \mathbf{C} renders the Lagrangian constitutive moduli \mathbf{L} ,

$$\mathbf{L} = 2 \frac{d\mathbf{S}(\mathbf{F}, \mathbf{F}^g)}{d\mathbf{C}} = 2 \frac{\partial \mathbf{S}}{\partial \mathbf{C}} \Big|_{\mathbf{F}^g} + 2 \left[\frac{\partial \mathbf{S}}{\partial \mathbf{F}^g} \Big|_{\mathbf{F}} : \frac{\partial \mathbf{F}^g}{\partial \vartheta^g} \right] \otimes \frac{\partial \vartheta^g}{\partial \mathbf{C}} \quad (18)$$

which are an essential ingredient for the global Newton iteration. The Lagrangian constitutive moduli \mathbf{L} consist of four terms. The first term $2\partial\mathbf{S}/\partial\mathbf{C}$

$$2 \frac{\partial \mathbf{S}}{\partial \mathbf{C}} = [\mathbf{F}^{g-1} \otimes \mathbf{F}^{g-1}] : \mathbf{L}^e : [\mathbf{F}^{g-t} \otimes \mathbf{F}^{g-t}] \quad (19)$$

is nothing but the pull back of the elastic moduli $\mathbf{L}^e = 2\partial\mathbf{S}^e/\partial\mathbf{C}^e$ introduced in Eq. (7) onto the reference configuration. The second term $\partial\mathbf{S}/\partial\mathbf{F}^g$

$$\frac{\partial\mathbf{S}}{\partial\mathbf{F}^g} = -[\mathbf{F}^{g-1}\otimes\mathbf{S} + \mathbf{S}\otimes\mathbf{F}^{g-1}] - [\mathbf{F}^{g-1}\otimes\mathbf{F}^{g-1}] : \frac{1}{2}\mathbf{L}^e : [\mathbf{F}^{g-t}\otimes\mathbf{C}^e + \mathbf{C}^e\otimes\mathbf{F}^{g-t}] \quad (20)$$

consists of two contributions that resemble a geometric and a material stiffness contribution similar to classical nonlinear computational mechanics. The third term $\partial\mathbf{F}^g/\partial\vartheta^g$

$$\frac{\partial\mathbf{F}^g}{\partial\vartheta^g} = \mathbf{f}_0 \otimes \mathbf{f}_0 \quad (21)$$

depends on the particular constitutive choice for the growth tensor (10) and the fourth term $\partial\vartheta^g/\partial\mathbf{C}$

$$\frac{\partial\vartheta^g}{\partial\mathbf{C}} = \frac{\partial\vartheta^g}{\partial\lambda} \frac{\partial\lambda}{\partial\mathbf{C}} = \left[\frac{k^g}{K} \Delta t \right] \left[\frac{1}{2\lambda} \mathbf{f}_0 \otimes \mathbf{f}_0 \right] \quad (22)$$

depends on the discrete formulation of the particular evolution equation (11) for the eccentric growth multiplier ϑ^g .

2.3. Stress-driven concentric growth

Next, we specify the generic growth equations from Section 2.1 to characterize pathophysiological concentric growth, which we model as a stress-driven, transversely isotropic, irreversible process. Motivated by physiological observations, we introduce a single scalar-valued growth multiplier $\vartheta^\perp = \vartheta^s$ that reflects the parallel deposition of sarcomeres associated with transverse cardiomyocyte growth on the microscopic scale, while there is no growth in the fiber and sheet plane normal directions, $\vartheta^f = \vartheta^n = 1$, see Fig. 5. The growth tensor can thus be expressed as a simple rank one-update of the identity tensor along the direction of the ventricular pressure which we assume to coincide with the direction of the sheet vector \mathbf{s}_0 :

$$\mathbf{F}^g = \mathbf{I} + [\vartheta^\perp - 1] \mathbf{s}_0 \otimes \mathbf{s}_0 \quad (23)$$

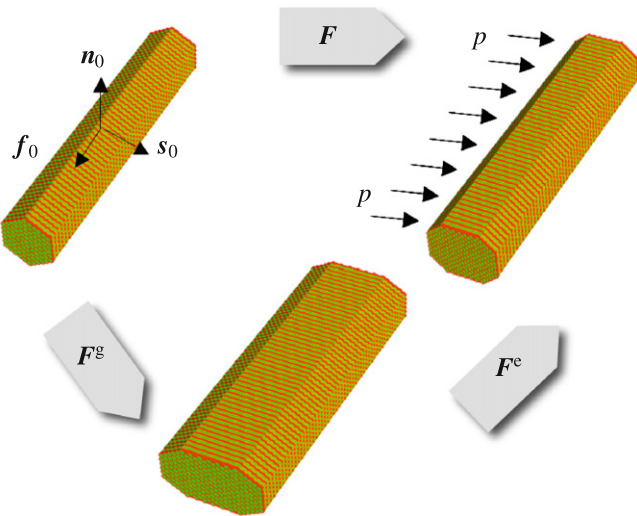


Fig. 5. Kinematics of concentric growth. Parallel sarcomere deposition induces concentric cardiomyocyte growth $\mathbf{F}^g = \mathbf{I} + [\vartheta^\perp - 1] \mathbf{s}_0 \otimes \mathbf{s}_0$ associated with cardiomyocyte thickening in the sheet direction \mathbf{s}_0 , i.e., along the direction of applied pressure. Sarcomere deposition is driven by a stress-driven growth criterion $\phi^\perp = \text{tr}(\mathbf{M}^e) - p^{\text{crit}}$, which is activated if the trace of the elastic Mandel stress $\text{tr}(\mathbf{M}^e)$, i.e., the current pressure p , exceeds a critical physiological pressure level p^{crit} . In the above example for $\vartheta^\perp = 2.0$, \mathbf{F}^g characterizes the parallel deposition of sarcomere units in the sheet direction inducing a doubling of the cell thickness from 16.7 to 33.3 μm . \mathbf{F}^c reflects a lateral pressure p at a constant number of sarcomere units, with the individual sarcomeres being compressed in the \mathbf{s}_0 direction.

Motivated by clinical observations, we introduce a stress-driven evolution equation for eccentric hypertrophic growth:

$$\dot{\vartheta}^\perp = k^\perp(\vartheta^\perp) \phi^\perp(\mathbf{M}^e) \quad (24)$$

To ensure that the cardiomyocytes do not thicken unboundedly, the growth criterion ϕ^\perp is scaled by the function k^\perp :

$$k^\perp = \frac{1}{\tau} \left[\frac{\vartheta^{\text{max}} - \vartheta^\perp}{\vartheta^{\text{max}} - 1} \right]^\gamma \quad \text{with} \quad \frac{\partial k^\perp}{\partial \vartheta^\perp} = -\frac{\gamma}{[\vartheta^{\text{max}} - \vartheta^\perp]} k^\perp \quad (25)$$

Again, the three characteristic material parameters of this scaling function all have a clear physical interpretation, τ denotes the sarcomere deposition time, γ calibrates the shape of the sarcomere deposition curve, i.e., the degree of nonlinearity of the growth process, and ϑ^{max} denotes the area fraction of maximum parallel sarcomere deposition. For example, a maximum parallel sarcomere deposition of $\vartheta^{\text{max}} = 2$ would allow for a possible doubling of the cardiomyocyte thickness from 16.7 to 33.3 μm , see Fig. 5. Lastly, we introduce a stress-driven concentric growth criterion ϕ^\perp :

$$\phi^\perp = \text{tr}(\mathbf{M}^e) - p^{\text{crit}} \quad \text{with} \quad \frac{\partial \phi^\perp}{\partial \vartheta^\perp} = \frac{\partial \mathbf{C}^e}{\partial \vartheta^\perp} : \mathbf{S}^e + \mathbf{C}^e : \frac{\partial \mathbf{S}^e}{\partial \vartheta^\perp} \quad (26)$$

Following an energetically conjugate approach, we choose the overstress $\text{tr}(\mathbf{M}^e) - p^{\text{crit}}$, i.e., the difference between the trace of the Mandel stress of the intermediate configuration $\mathbf{M}^e = \mathbf{C}^e \cdot \mathbf{S}^e$ and the critical physiological pressure level p^{crit} as the driving force for growth (Epstein and Maugin, 2000; Himpel et al., 2005). Conceptually speaking, $\text{tr}(\mathbf{M}^e)$ equals the trace of the Kirchhoff stress which is nothing but the Cauchy stress weighted by the Jacobian. In contrast to strain-driven eccentric growth, the sensitivities for stress-driven concentric growth (25.2) and (26.2), which will become essential for the consistent algorithmic linearization, are slightly more complex and require the calculation of the following derivatives:

$$\frac{\partial \mathbf{C}^e}{\partial \vartheta^\perp} = -\mathbf{F}^{g-t} \cdot \frac{\partial \mathbf{F}^{g-t}}{\partial \vartheta^\perp} \cdot \mathbf{C}^e - \mathbf{C}^e \cdot \frac{\partial \mathbf{F}^{g-t}}{\partial \vartheta^\perp} \cdot \mathbf{F}^{g-1}$$

$$\frac{\partial \mathbf{S}^e}{\partial \vartheta^\perp} = \frac{1}{2} \mathbf{L}^e : \frac{\partial \mathbf{C}^e}{\partial \vartheta^\perp} \quad (27)$$

Again, we apply an implicit Euler backward scheme with

$$\dot{\vartheta}^\perp = [\vartheta^\perp - \vartheta_n^\perp] / \Delta t \quad (28)$$

to obtain the following expression for the discrete local residual:

$$\mathbf{R}^\perp = \vartheta^\perp - \vartheta_n^\perp - \frac{1}{\tau} \left[\frac{\vartheta^{\text{max}} - \vartheta^\perp}{\vartheta^{\text{max}} - 1} \right]^\gamma [\text{tr}(\mathbf{M}^e) - M^{\text{e crit}}] \Delta t \approx 0 \quad (29)$$

The iterative update of the concentric growth multiplier $\vartheta^\perp \leftarrow \vartheta^\perp - \mathbf{R}^\perp / \mathbf{K}^\perp$ can then be expressed in terms of the linearization of discrete residual (29),

$$\mathbf{K}^\perp = \frac{d\mathbf{R}^\perp}{d\vartheta^\perp} = 1 - \left[k^g \frac{\partial \phi^g}{\partial \vartheta^\perp} + \phi^g \frac{\partial k^g}{\partial \vartheta^\perp} \right] \Delta t \quad (30)$$

with the individual terms given in (25)–(27). Upon convergence of ϑ^\perp , we can successively update the growth tensor $\mathbf{F}^g = \mathbf{I} + [\vartheta^\perp - 1] \mathbf{s}_0 \otimes \mathbf{s}_0$ from Eq. (23), the elastic tensor $\mathbf{F}^e = \mathbf{F} \cdot \mathbf{F}^{g-1}$ from Eq. (1), the elastic stress $\mathbf{S}^e = 2\partial\psi/\partial\mathbf{C}^e$ from Eq. (6), and the second

Piola Kirchhoff stress \mathbf{S} from Eq. (6)

$$\mathbf{S} = \mathbf{F}^{\mathbf{g}-1} \cdot \mathbf{S}^e \cdot \mathbf{F}^{\mathbf{g}-t} \quad \text{with} \quad \mathbf{S}^e = 2 \frac{\partial \psi}{\partial \mathbf{C}^e} \quad (31)$$

to finally evaluate the global equilibrium equation (3). Similar to the eccentric growth case, the stress linearization with respect to the total right Cauchy Green tensor \mathbf{C} renders the Lagrangian constitutive moduli \mathbf{L} for the global Newton iteration:

$$\mathbf{L} = 2 \frac{d\mathbf{S}(\mathbf{F}, \mathbf{F}^{\mathbf{g}})}{d\mathbf{C}} = 2 \frac{\partial \mathbf{S}}{\partial \mathbf{C}} \Big|_{\mathbf{F}^{\mathbf{g}}} + 2 \left[\frac{\partial \mathbf{S}}{\partial \mathbf{F}^{\mathbf{g}}} \Big|_{\mathbf{F}} : \frac{\partial \mathbf{F}^{\mathbf{g}}}{\partial \vartheta^\perp} \right] \otimes \frac{\partial \vartheta^\perp}{\partial \mathbf{C}} \quad (32)$$

The first term $2\partial\mathbf{S}/\partial\mathbf{C}$

$$2 \frac{\partial \mathbf{S}}{\partial \mathbf{C}} = [\mathbf{F}^{\mathbf{g}-1} \otimes \mathbf{F}^{\mathbf{g}-1}] : \mathbf{L}^e : [\mathbf{F}^{\mathbf{g}-t} \otimes \mathbf{F}^{\mathbf{g}-t}] \quad (33)$$

and the second term $\partial\mathbf{S}/\partial\mathbf{F}^{\mathbf{g}}$

$$\frac{\partial \mathbf{S}}{\partial \mathbf{F}^{\mathbf{g}}} = -[\mathbf{F}^{\mathbf{g}-1} \otimes \mathbf{S} + \mathbf{S} \otimes \mathbf{F}^{\mathbf{g}-1}] - [\mathbf{F}^{\mathbf{g}-1} \otimes \mathbf{F}^{\mathbf{g}-1}] : \frac{1}{2} \mathbf{L}^e : [\mathbf{F}^{\mathbf{g}-t} \otimes \mathbf{C}^e + \mathbf{C}^e \otimes \mathbf{F}^{\mathbf{g}-t}] \quad (34)$$

are generic terms that do not depend on the particular growth law. They are thus identical to the case of eccentric growth case in (19) and (20). The third term

$$\frac{\partial \mathbf{F}^{\mathbf{g}}}{\partial \vartheta^\perp} = \mathbf{s}_0 \otimes \mathbf{s}_0 \quad (35)$$

which depends on the particular constitutive choice for the growth tensor (23) is nothing but the structural tensor $\mathbf{s}_0 \otimes \mathbf{s}_0$. The fourth term contains the partial derivative of the converged growth multiplier ϑ^\perp with respect to the right Cauchy Green tensor of the reference configuration \mathbf{C} :

$$\frac{\partial \vartheta^\perp}{\partial \mathbf{C}} = \frac{\partial \vartheta^\perp}{\partial \mathbf{C}^e} : \frac{\partial \mathbf{C}^e}{\partial \mathbf{C}} = \left[\frac{k^{\mathbf{g}}}{K} \Delta t \right] \left[\frac{1}{2} \mathbf{C} : \mathbf{L}^0 + \mathbf{S} \right] \quad (36)$$

This term is a bit more complex than its strain-driven counterpart (22). For the sake of brevity, we have introduced the abbreviation $\mathbf{L}^0 = [\mathbf{F}^{\mathbf{g}-1} \otimes \mathbf{F}^{\mathbf{g}-1}] : \mathbf{L}^e : [\mathbf{F}^{\mathbf{g}-t} \otimes \mathbf{F}^{\mathbf{g}-t}]$ for the pull back of the elastic moduli $\mathbf{L}^e = 2\partial\mathbf{S}^e/\partial\mathbf{C}^e$ from the grown intermediate configuration to the undeformed reference configuration.

3. Results

In this section, we explore the basic features of the strain-driven eccentric model and the stress-driven concentric model for cardiac growth. We compare both models using a generic bi-ventricular heart geometry that we briefly outline at the beginning of this section.

3.1. Generic bi-ventricular heart model

To avoid geometric effects resulting from complex patient-specific geometries, we explore our new multiscale algorithm using the generic bi-ventricular heart model illustrated in Fig. 6. In this prototype model, the left and right ventricles, the lower chambers of the heart, are represented through two truncated ellipsoids with heights of 70 and 60 mm, and radii of 30 and 51 mm, respectively, such that the right ventricle blends smoothly into the left ventricle from apex to base (Göktepe et al., 2010a). The left ventricle which pumps oxygenated blood into the body operates at a pressure of 100 mmHg. The right ventricle pumps deoxygenated blood into the lungs at a pressure of 20 mmHg (Göktepe et al., 2010b). With 12 mm, the left ventricular wall is thicker and its muscle is significantly stronger than the 6 mm thick right ventricular wall. For the lack of better knowledge, we apply homogeneous Dirichlet boundary conditions to all nodes on the basal plane. In addition, to mimic the boundary conditions

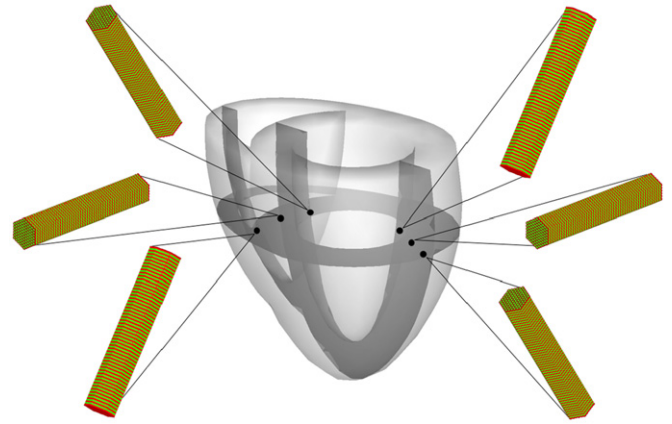


Fig. 6. Generic bi-ventricular heart model generated from two truncated ellipsoids (Göktepe et al., 2010a), with heights of 70 and 60 mm, radii of 30 and 51 mm, and wall thicknesses of 12 and 6 mm, respectively. In the healthy heart, cardiomyocytes are assumed to be cylindrical, 100 μm long with a diameter of 16.7 μm . They consist of 50 serial sarcomere units in length and 91 parallel units per cross section, each of them 2 μm long and 2 μm in diameter. They are arranged helically around the long axis of the heart with a transmurally varying inclination of -55° in the epicardium, the outer wall, to $+55^\circ$ in the endocardium, the inner wall, measured with respect to the basal plane.

imposed by the surrounding tissue, we support all nodes of the epicardium by linear springs with a stiffness of $k=10^{-3}$ N/mm both in the radial and tangential directions. The generic bi-ventricular heart model is discretized with 3910 linear tetrahedral elements connected at 1028 nodes. In the healthy heart, cardiomyocytes are assumed to be cylindrical, 100 μm long with a diameter of 16.7 μm . They consist of 50 serial sarcomere units in length and 91 parallel units per cross section, each of them 2 μm long and 2 μm in diameter. The individual cardiomyocytes are arranged helically around the ventricles. Here, we assume that the fiber directions \mathbf{f}_0 vary transmurally from an inclination of -55° in the epicardium, the outer wall, to $+55^\circ$ in the endocardium, the inner wall, where the inclination is measured with respect to the basal plane, see Fig. 6. The inclination is assumed to decay gradually from base to apex towards a final value of 0° . For the sake of simplicity, the myocardial sheet directions \mathbf{s}_0 are assumed to be oriented normal to the endocardium and epicardium. To focus on the impact of growth, we assume a generic isotropic Neo-Hookean baseline elasticity and specify the free energy as $\psi = \frac{1}{2} \lambda \ln^2(J^e) + \frac{1}{2} \mu [\mathbf{C}^e : \mathbf{I} - 3 - 2 \ln(J^e)]$. According to Eq. (6), the elastic second Piola Kirchhoff stress $\mathbf{S}^e = 2\partial\psi/\partial\mathbf{C}^e$ can then be expressed as $\mathbf{S}^e = [\lambda \ln(J^e) - \mu] \mathbf{C}^{e-1} + \mu \mathbf{I}$, and the elastic constitutive moduli $\mathbf{L}^e = 2\partial\mathbf{S}^e/\partial\mathbf{C}^e$ introduced in Eq. (7) take the following explicit representation $\mathbf{L}^e = \lambda \mathbf{C}^{e-1} \otimes \mathbf{C}^{e-1} + [\mu - \lambda \ln(J^e)] [\mathbf{C}^e \otimes \mathbf{C}^e + \mathbf{C}^e \otimes \mathbf{C}^e]$. The Lamé parameters for the baseline elastic response are chosen to be $\lambda = 0.577$ MPa and $\mu = 0.385$ MPa. The extension of the model to a more physiological orthotropic baseline elasticity along the fiber, sheet, and sheet plane normal directions, however, is straightforward and would only affect the calculation of the elastic second Piola Kirchhoff stress $\mathbf{S}^e = 2\partial\psi/\partial\mathbf{C}^e$ and the corresponding elastic constitutive moduli $\mathbf{L}^e = 2\partial\mathbf{S}^e/\partial\mathbf{C}^e$ (Göktepe et al., 2010a; Holzapfel and Ogden, 2009). We apply the following limiting growth function $k(\vartheta) = [(\vartheta^{\max} - \vartheta)/(\vartheta^{\max} - 1)]^\gamma / \tau$ for both eccentric and concentric growth (Lubarda and Hoger, 2002). For this function, the growth rate $\dot{\vartheta}$ decays smoothly until the growth multiplier ϑ has reached its maximum value ϑ^{\max} , while the sarcomere deposition time and the deposition nonlinearity are characterized through τ and γ , respectively (Göktepe et al., 2010c). We choose the sarcomere deposition time to $\tau = 3.2$ MPa s and the deposition nonlinearity

to $\gamma = 2.0$, but denote that at this point their choice is relatively generic since they only affect the speed of growth, but not the end result. In the future, however, we will use these two parameters to calibrate our model against long-term chronic clinical observations. All the above features will be the basis for the examples in Sections 3.2 and 3.3 to allow for a direct comparison of the two different growth models.

3.2. Strain-driven eccentric growth

The following example documents our attempts to simulate strain-driven eccentric growth in terms of the equations introduced in Section 2.2 using the generic bi-ventricular heart model, the loading and boundary conditions, and the material parameters outlined in Section 3.1. In addition, we need to specify two additional growth parameters, the physiological strain threshold $\lambda^{\text{crit}} = 1.01$ above which growth is activated and the maximum growth value $\vartheta^{\text{max}} = 1.50$. Fig. 7 illustrates the heterogeneous distribution of eccentric growth with a clear transmural variation

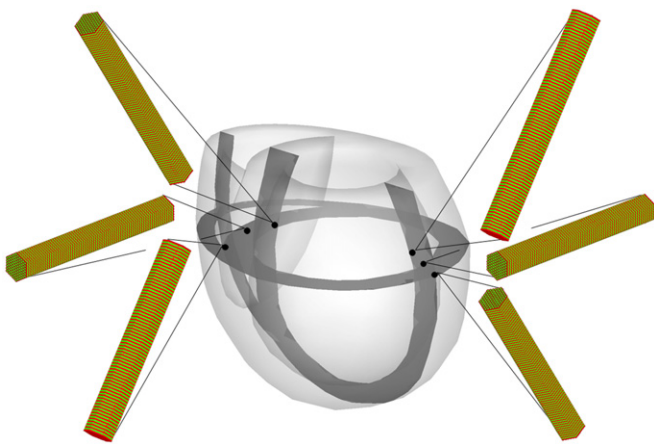


Fig. 7. Strain-driven eccentric growth. Overall, eccentric growth is clearly heterogeneous with a transmural variation in serial sarcomere deposition. Cardiomyocytes in the endocardium, the inner wall, reach their maximum length of $150\ \mu\text{m}$ through the serial deposition of 25 additional sarcomere units of $2\ \mu\text{m}$ each. Cardiomyocytes in the epicardium, the outer wall, reach a stable state at a length of $130\ \mu\text{m}$ through the serial deposition of 15 additional sarcomere units. Eccentric growth along the septum is almost identical to eccentric growth along the free wall initiating an overall shape change from elliptical to spherical.

in serial sarcomere deposition. Cardiomyocytes located in the endocardium, the inner wall, reach their maximum length of $150\ \mu\text{m}$ through the serial deposition of 25 additional sarcomere units with a length of $2\ \mu\text{m}$ each. Cardiomyocytes located in the epicardium, the outer wall, reach a stable state at a length of $130\ \mu\text{m}$ through the serial deposition of 15 additional sarcomere units. The temporal evolution of eccentric growth is illustrated in Fig. 8. Strain-driven eccentric growth manifests itself in a significant increase in cavity size while the wall thickness remains virtually unaltered. As growth progresses, the eccentric growth multiplier ϑ^{\parallel} gradually increases from its baseline value of $\vartheta^{\parallel} = 1.00$ to its maximum value of $\vartheta^{\parallel} = 1.50$ as additional sarcomeres are deposited in series to allow the individual cardiomyocytes to grow in the longitudinal direction. In accordance with Fig. 7, the growth multiplier takes its maximum value of $\vartheta^{\parallel} = \vartheta^{\text{max}} = 1.50$ at the inner wall of the horizontal section, while the outer wall displays a slightly lower value of $\vartheta^{\parallel} = \vartheta^{\text{max}} = 1.30$. Although eccentric growth may vary across the ventricular wall, growth along the septum is almost identical to growth along the free wall. The eccentric growth multiplier ϑ^{\parallel} is largest at the endocardium, the inner wall, and smallest at the epicardium, the outer wall. Since the base is supported through Dirichlet boundary conditions, growth is constrained around the annulus region. Overall, eccentric growth is smallest at the base and at the apex, and largest in the midsection, initiating a shape change from elliptical to spherical (Cheng et al., 2006). The strain-driven eccentric growth simulation illustrated in Fig. 8 is excellent qualitative agreement with the pathophysiological characteristics of volume-overload induced cardiac dilation (Kumar et al., 2005): (i) a progressive increase in cardiac diameter and mass, (ii) an alteration of cardiac form from elliptical to spherical, (iii) a relatively constant wall thickness, and (iv) a significant increase of the apex to base distance.

3.3. Stress-driven concentric growth

Our second example illustrates the performance of our growth model in the context of stress-driven concentric growth using our generic bi-ventricular heart model. Again, the geometry, boundary conditions, and loading are adopted from Section 3.1. The two additional growth parameters are the physiological threshold pressure $p^{\text{crit}} = 0.012\ \text{MPa}$ and the maximum growth threshold $\vartheta^{\text{max}} = 3.00$. Fig. 9 demonstrates the heterogeneous perpendicular sarcomere deposition within the individual cardiomyocytes with

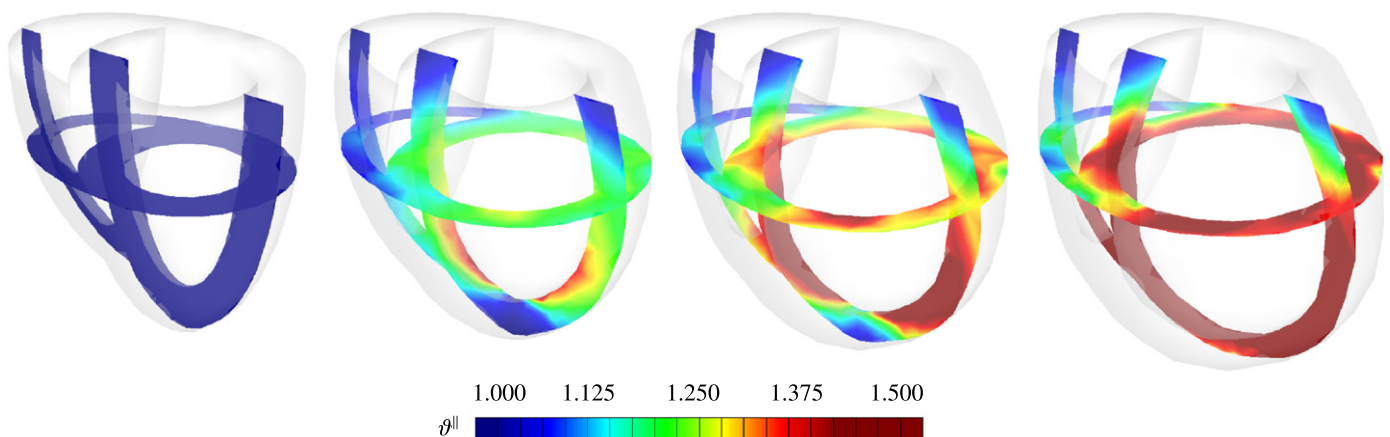


Fig. 8. Strain-driven eccentric growth. The eccentric growth multiplier ϑ^{\parallel} gradually increases from 1.00 to 1.50 as the individual cardiomyocytes grow eccentrically. On the structural level, eccentric growth manifests itself in a progressive dilation of the left ventricle accompanied by a significant increase in cardiac mass, while the thickness of the ventricular wall remains virtually unchanged.

a maximum sarcomere deposition in the epicardium, the outer wall. Cardiomyocytes located in the epicardium reach their maximum thickness of $50\mu\text{m}$ through the parallel deposition of 182 sarcomere units at $\vartheta^\perp = \vartheta^{\text{max}} = 3.0$. Cardiomyocytes located in the endocardium, the inner wall, reach a stable state at a thickness of $31.4\mu\text{m}$ through the parallel deposition of 84 additional sarcomere units reflected through $\vartheta^\perp = 1.92$. Since the septal wall receives structural support through the pressure in the right ventricle, concentric growth at the septal wall is slightly less pronounced than at the free wall. Fig. 10 illustrates the temporal evolution of the growth multiplier ϑ^\perp which increases from 1.00 to 3.00 as the individual cardiomyocytes grow concentrically. On the structural level, concentric growth manifests itself in a progressive transmural wall thickening to withstand higher blood pressure levels while the overall size of the heart remains virtually unchanged. In contrast to the example of strain driven eccentric growth, concentric growth starts at the outer wall, and is more pronounced at the free wall than at the septum. This is in excellent agreement with experimental findings

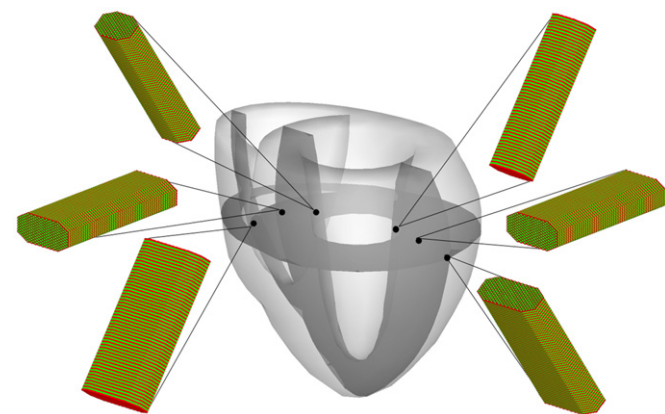


Fig. 9. Stress-driven concentric growth. Concentric growth is clearly heterogeneous with a transmural variation in parallel sarcomere deposition. Cardiomyocytes in the endocardium, the inner wall, reach a stable state at a thickness of $31.4\mu\text{m}$ through the parallel deposition of 84 additional sarcomere units. Cardiomyocytes in the epicardium, the outer wall, reach their maximum thickness of $50\mu\text{m}$ through the parallel deposition of 182 sarcomere units. Concentric growth at the free wall is slightly more pronounced than at the septum.

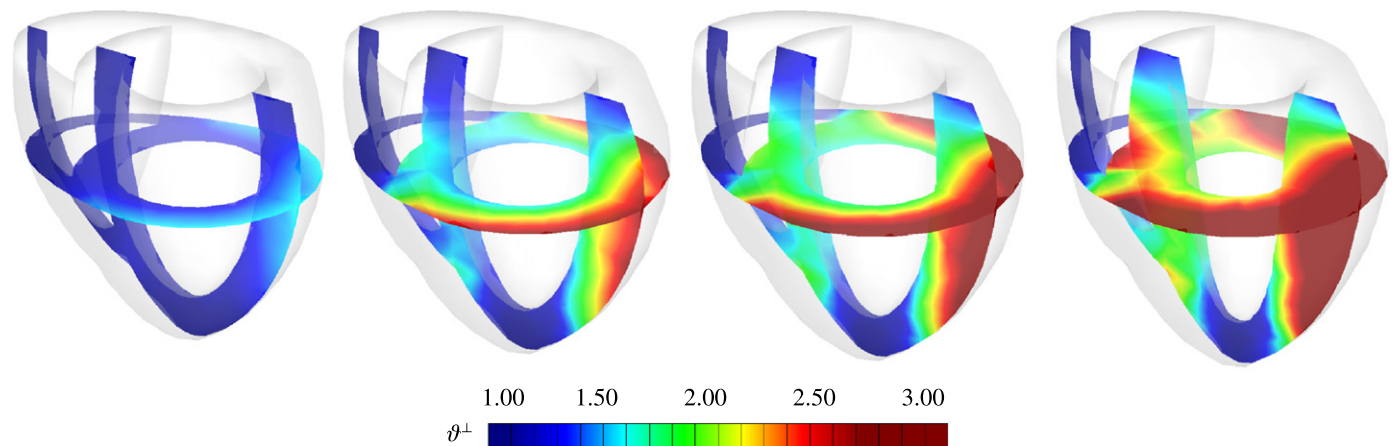


Fig. 10. Stress-driven concentric growth. The concentric growth multiplier ϑ^\perp gradually increases from 1.00 to 3.00 as the individual cardiomyocytes grow concentrically. On the structural level, concentric growth manifests itself in a progressive transmural wall thickening to withstand higher blood pressure levels while the overall size of the heart remains virtually unaffected. Since the septal wall receives structural support through the pressure in the right ventricle, wall thickening is slightly more pronounced in the free wall where the wall stresses are higher.

that reported a regional variation in cell thickening with a more pronounced concentric growth in the free wall as compared to the septum, and with a more pronounced cell thickening in the epicardium as compared to the endocardium (Smith and Bishop, 1985). In summary, the stress-driven concentric growth simulation illustrated in Fig. 10 is in excellent qualitative agreement with the pathophysiological characteristics of cardiac wall thickening: (i) a progressive wall thickening, (ii) a relatively constant heart size, and (iii) a potential occlusion of the outflow tract through pronounced septal growth.

4. Discussion

Eccentric and concentric cardiac growth are serious maladaptive conditions in which the heart muscle undergoes chronic volumetric changes in response to alterations in its mechanical environment. In this manuscript, we have developed a novel multiscale model for strain-driven eccentric growth and stress-driven concentric growth and demonstrated its computational realization within a geometrically nonlinear finite element framework. We have adopted the commonly accepted framework for volumetric growth based on the multiplicative decomposition of the deformation gradient $\mathbf{F} = \mathbf{F}^e \cdot \mathbf{F}^g$ into an elastic part \mathbf{F}^e and a growth part \mathbf{F}^g . Our model is based on the key kinematic assumption that the individual cardiomyocytes deform affinely with the surrounding myocardial tissue. This allowed us to introduce the growth tensor \mathbf{F}^g and its evolution equations in terms of morphological changes of the individual cardiomyocytes induced by the generation and deposition of novel sarcomere units. A recent study exploring cardiomyocytes with different length to thickness ratios confirms the close correlation between cardiomyocyte shape and intracellular sarcomeric architecture (Bray et al., 2008; Geisse et al., 2009), which is the basic paradigm for the proposed model.

4.1. Strain-driven eccentric growth

We have presented a novel multiscale continuum model for pathological eccentric growth as a strain-driven, transversely isotropic, irreversible process. Its growth tensor \mathbf{F}^g is defined as a rank-one update of the unity tensor in terms of the eccentric growth multiplier ϑ^\parallel acting along the cell's long axis \mathbf{f}_0 .

On the molecular level, eccentric growth, which can be interpreted as serial sarcomere deposition, is activated once the elastic cardiomyocyte stretch λ^e exceeds a critical physiological threshold level λ^{crit} . When experimentally subjected to uniaxial overstretch, isolated cardiomyocytes have been reported to display an acute sarcomere lengthening *in vitro* (Mansour et al., 2004). However, it is well-accepted that a constant sarcomere length is required for optimal tension development. In an attempt to maintain maximum force generation, sarcomeres are reported to recover their optimal resting length of 1.9–2.1 μm through new protein synthesis within a couple of hours. This effect is inherently incorporated in the present model.

On the cellular level, the evolution of eccentric growth is governed by the growth criterion $\phi^l = \lambda^e - \lambda^{crit}$ scaled by a growth function k^l parameterized in terms of three material constants. In contrast to phenomenological growth laws reported in the literature (Ambrosi et al., 2009), our three material parameters ϑ^{max} , τ , and γ have a clear physical interpretation. The maximum serial sarcomere deposition which we have chosen to $\vartheta^{max} = 1.5$ ensures that cardiomyocytes do not lengthen unboundedly. In freshly isolated cardiac tissue, compared with a healthy control group, cardiomyocytes from patients with dilated cardiomyopathy were reported to be 40% longer, while the cell widths displayed no statistically significant differences. The length of the individual sarcomeres, however, was the same in both groups (Gerdes et al., 1992). This is in excellent agreement with the effects captured by our model as demonstrated in Fig. 7. In our model, the temporal evolution of the serial sarcomere deposition is governed through two parameters, the sarcomere deposition time τ and the sarcomere deposition nonlinearity γ . Since we were only interested in the final converged end result of growth, the values of these parameters did not play a key role in the present analysis. A recent *in vivo* study of volume-overload in rabbits suggests that cardiomyocytes are able to add approximately one sarcomere per day and that the initial linearity of sarcomere deposition decays after approximately four weeks (Yoshida et al., 2010). We are currently calibrating the parameters τ and γ based on the serial sarcomere increase from 62 to 95 units during the 16-week long experiment reported in this study. Recent attempts to decipher the pathways of mechanotransduction during hypertrophic cardiomyopathy explore the role of the extracellular matrix on sarcomerogenesis (Parker et al., 2008) and force generation (Tracqui et al., 2008), and might provide further guidelines for a refinement of our model.

On the macroscopic level, maladaptive cardiomyocyte elongation manifests itself in the dilation of the left ventricle, a change in ventricular shape from elliptical to spherical, and a decrease in ejection fraction, while the wall thickness typically remains unaltered (Kumar et al., 2005; Opie, 2003). These effects are nicely captured by the present model as documented in Fig. 8.

4.2. Stress-driven concentric growth

Upon slight modifications, our generic continuum growth model has also been able to capture pathological concentric growth, which we have represented as a stress-driven, transversely isotropic, irreversible process. Similar to eccentric growth, its growth tensor \mathbf{F}^c is defined as a rank-one update of the unity tensor, this time parameterized in terms of the concentric growth multiplier ϑ^+ acting along the sheet direction \mathbf{s}_0 . On the molecular level, concentric growth is characterized through a parallel deposition of sarcomere units. It is activated once the trace of the Mandel stress of the intermediate configuration $\text{tr}(\mathbf{M}^e)$ exceeds a physiological pressure level p^{crit} . Experimentally

induced stress-driven hypertrophic wall thickening in ferrets revealed a regional variation in cell thickening with a more pronounced concentric growth in the free wall as compared to the septum, and with a more pronounced cell thickening in the epicardium as compared to the endocardium (Smith and Bishop, 1985). This regional variation is in excellent agreement with our prediction of the parallel sarcomere deposition illustrated in Fig. 9. It corresponds nicely to the spatial distribution of the concentric growth multiplier ϑ^+ documented in Fig. 10.

On the cellular level, the evolution of concentric growth is governed by the growth criterion $\phi^+ = \text{tr}(\mathbf{M}^e) - p^{crit}$ scaled by a growth function k^+ , again parameterized in terms of three material constants. The maximum parallel sarcomere deposition which we have chosen to $\vartheta^{max} = 3.0$ ensures that cardiomyocytes do not thicken unboundedly. This is in nice agreement with the relative increase in transverse cardiomyocyte diameters from 15 μm up to 40 μm reported for pressure-overload induced hypertrophic cardiomyopathy (Kumar et al., 2005).

On the macroscopic level, concentric cardiomyocyte growth has been reported to potentially translate into wall thicknesses of more than 3 cm, while the overall size of the heart might remain virtually unaffected (Maron and McKenna, 2003). This is in excellent quantitative agreement with the computationally predicted wall thickness and the overall cardiac size documented in Fig. 10.

4.3. Summary

The central goal of this manuscript was the introduction of a generic model for eccentric and concentric growth that allows exploration of the impact of growth on different scales. For the sake of transparency, we have modeled the baseline properties of cardiac tissue as isotropic and passive. However, we are currently extending the model to incorporate a more physiological orthotropic baseline elasticity for the passive myocardium parameterized in terms of the fiber, sheet, and sheet plane normal directions (Göktepe et al., 2010a; Holzapfel and Ogden, 2009). Along the lines of a true multiscale approach, the response along the fiber direction can then be calibrated by means of experimentally measured length–tension relations. Moreover, we are in the process of including electrically activated contraction for the individual cardiomyocytes to explore the long-term impact of alterations in active and passive stress on cardiac growth (Göktepe and Kuhl, 2009, 2010; Göktepe et al., 2010d; Kotikanyadanam et al.). For more realistic simulations, it would also be essential to begin the simulation with a loaded state at growth equilibrium and include effects of residual stress (Omens et al., 1998; Rodriguez et al., 1994). Hypertrophy would then be triggered by changes in loads from this equilibrium state. Taken altogether, this will allow us to predict the overall impact of eccentric and concentric growth on clinically relevant global metrics of cardiac function, such as the end systolic and end diastolic volumes and the ejection fraction. Overall, we believe that our cardiac growth model has tremendous potential in helping to predict, and potentially prevent, maladaptive growth of the heart. We have demonstrated that it is in excellent agreement with experimental findings on the modelular (sarcomere), cellular (cardiomyocyte), tissue (myocardium), and organ (heart) levels.

Acknowledgements

We acknowledge contributions by Nicholas Geisse from the Disease Biophysics group at Harvard. The material of this manuscript is based on work supported by the National Science Foundation CAREER award CMMI-0952021 “The Virtual

Heart - Exploring the structure-function relationship in electro-active cardiac tissue”, by the Hellman Faculty Scholars grant “A predictive multiscale simulation tool for heart failure”, by the Stanford Bio-X grant “An integrated approach to cardiac repair: Predictive computational models, engineered biomaterials, and stem cells”, and by the National Science Foundation ERFI program through Grant EFRI-CBE-0735551 “Engineering of cardiovascular cellular interfaces and tissue constructs”.

References

- Alford, P.W., Taber, L.A., 2008. Computational study of growth and remodelling in the aortic arch. *Comput. Methods. Biomech. Biomed. Eng.* 11, 525–538.
- Ambrosi, D., Mollica, F., 2002. On the mechanics of a growing tumor. *Int. J. Eng. Sci.* 40, 1297–1316.
- Ambrosi, D., Ateshian, G.A., Arruda, E.M., Ben Amar, M., Cowin, S.C., Dumais, J., Goriely, A., Holzapfel, G.A., Humphrey, J.D., Kemkemer, R., Kuhl, E., Ma, J., Olberding, J.E., Taber, L.A., Vandiver, R., Garikipati, K., 2010. Perspectives on biological growth and remodeling, under review.
- Berne, R.M., Levy, M.N., 2001. *Cardiovascular Physiology*. The Mosby Monograph Series.
- Boyce, M.C., Weber, G.G., Parks, D.M., 1989. On the kinematics of finite strain plasticity. *J. Mech. Phys. Solids* 37, 647–665.
- Bray, M.A., Sheehy, S.P., Parker, K.K., 2008. Sarcomere alignment is regulated by myocyte shape. *Cell Motility Cytoskel.* 65, 641–651.
- Cheng, A., Nguyen, T.C., Malinowski, M., Ennis, D.B., Daughters, G.T., Miller, D.C., Ingels, N.B., 2006. Transmural left ventricular shear strain alterations adjacent to and remote from infarcted myocardium. *J. Heart Valve Dis.* 15, 209–218.
- Cox, B., 2010. A multi-scale, discrete-cell simulation of organogenesis: application to the effects of strain stimulus on collective cell behavior during ameloblast migration. *J. Theor. Biol.* 262, 58–72.
- Emmanouilides, G.C., Riemenschneider, R.A., Allen, H.D., Gutgesell, H.P., 1994. *Moss and Adams' Heart Disease in Infants, Children, and Adolescents*, fifth ed. Lippincott Williams & Wilkins, Philadelphia.
- Epstein, M., Maugin, G.A., 2000. Thermomechanics of volumetric growth in uniform bodies. *Int. J. Plast.* 16, 951–978.
- Garikipati, K., 2009. The kinematics of biological growth. *Appl. Mech. Rev.* 62 030801-1–030801-7.
- Geisse, N.A., Sheehy, S.P., Parker, K.K., 2009. Control of myocyte remodeling in vitro with engineered substrates. *In Vitro Cell Dev. Bio. Animal* 45, 343–350.
- Gerdes, A.M., Kellerman, S.E., Moore, J.A., Muffly, K.E., Clark, L.C., Reaves, P.Y., Malec, K.B., Mc Keown, P.P., Schocken, D.D., 1992. Structural remodeling of cardiac myocytes in patients with ischemic cardiomyopathy. *Circulation* 86, 426–430.
- Gerdes, A.M., Capasso, J.M., 1995. Structural remodeling and mechanical dysfunction of cardiac myocytes in heart failure. *J. Mol. Cell Cardiol.* 27, 849–856.
- Gerdes, A.M., 2002. Cardiac myocyte remodeling in hypertrophy and progression to failure. *J. Card. Fail.* 8, S264–S268.
- Göktepe, S., Kuhl, E., 2009. Computational modeling of cardiac electrophysiology: a novel finite element approach. *Int. J. Numer. Methods Eng.* 79, 156–178.
- Göktepe, S., Kuhl, E., 2010. Electromechanics of cardiac tissue: a unified approach to the fully coupled excitation-contraction problem. *Comput. Mech.* 45, 227–243.
- Göktepe, S., Acharya, S.N.S., Wong, J., Kuhl, E., 2010a. Computational modeling of passive myocardium. *Int. J. Numer. Meth. Biomed. Eng.*, in press.
- Göktepe, S., Bothe, W., Kvitting, J.P., Swanson, J.C., Ingels, N.B., Miller, D.C., Kuhl, E., 2010b. Anterior mitral leaflet curvature in the beating ovine heart: a case study using videofluoroscopic markers and subdivision surfaces. *Biomech. Mod. Mechanobiol.*, doi:10.1007/s10237-009-0176-z.
- Göktepe, S., Abilez, O., Kuhl, E., 2010c. A generic approach towards finite growth with examples of athlete's heart, cardiac dilation, and cardiac wall thickening, under review.
- Göktepe, S., Wong, J., Kuhl, E., 2010d. Atrial and ventricular fibrillation—computational simulation of spiral waves in cardiac tissue. *Arch. Appl. Mech.* 80, 569–580.
- Goriely, A., Tabor, M., 2003. Biomechanical models of hyphal growth in actinomyces. *J. Theor. Biol.* 222, 211–218.
- Goriely, A., Ben Amar, M., 2007. On the definition and modeling of incremental, cumulative, and continuous growth laws in morphoelasticity. *Biomech. Mod. Mechanobiol.* 6, 289–296.
- Himpel, G., Kuhl, E., Menzel, A., Steinmann, P., 2005. Computational modeling of isotropic multiplicative growth. *Comput. Mod. Eng. Sci.* 8, 119–134.
- Himpel, G., Menzel, A., Kuhl, E., Steinmann, P., 2008. Time-dependent fibre reorientation of transversely isotropic continua—finite element formulation and consistent linearization. *Int. J. Numer. Methods Eng.* 73, 1413–1433.
- Holzapfel, G.A., Ogden, R.W., 2009. Constitutive modelling of passive myocardium. A structurally-based framework for material characterization. *Philos. Trans. R. Soc. London A* 367, 3445–3475.
- Humphrey, J.D., 2002. *Cardiovascular Solid Mechanics*. Springer Verlag, Berlin, Heidelberg, New York.
- Hunter, J.J., Chien, K.R., 1999. Signaling pathways for cardiac hypertrophy and failure. *New England J. Med.* 341, 1276–1283.
- Kotikanyadanam, M., Göktepe, S., Kuhl, E., 2010. Computational modeling of electrocardiograms: a finite element approach towards cardiac excitation. *Int. J. Numer. Methods Biomed. Eng.* 26, 524–533.
- Kroon, W., Delhaas, T., Arts, T., Bovendeerd, P., 2009. Computational modeling of volumetric soft tissue growth: application to the cardiac left ventricle. *Biomech. Mod. Mechanobiol.* 8, 309–310.
- Kuhl, E., Steinmann, P., 2003a. Mass- and volume specific views on thermodynamics for open systems. *Proc. R. Soc.* 459, 2547–2568.
- Kuhl, E., Steinmann, P., 2003b. On spatial and material settings of thermohyperelastodynamics for open systems. *Acta Mech.* 160, 179–217.
- Kuhl, E., Garikipati, K., Arruda, E.M., Grosh, K., 2005. Remodeling of biological tissue: mechanically induced reorientation of a transversely isotropic chain network. *J. Mech. Phys. Solids* 53, 1552–1573.
- Kuhl, E., Maas, R., Himpel, G., Menzel, A., 2007. Computational modeling of arterial wall growth: attempts towards patient-specific simulations based on computer tomography. *Biomech. Mod. Mechanobiol.* 6, 321–331.
- Kuhl, E., Holzapfel, G.A., 2007. A continuum model for remodeling in living structures. *J. Mater. Sci.* 2, 8811–8823.
- Kumar, V., Abbas, A.K., Fausto, N., 2005. *Robbins and Cotran Pathologic Basis of Disease*. Elsevier Saunders, Philadelphia.
- Lee, E.H., 1969. Elastic-plastic deformation at finite strains. *J. Appl. Mech.* 36, 1–6.
- Libby, P., Bonow, R.O., Mann, D.L., Zipes, D.P., 2007. *Braunwald's Heart Disease*. Elsevier Saunders, Philadelphia.
- Lubarda, A., Hoger, A., 2002. On the mechanics of solids with a growing mass. *Int. J. Solids Struct.* 39, 4627–4664.
- Mansour, H., de Tombe, P.P., Samarel, A.M., Russel, B., 2004. Restoration of resting sarcomere length after uniaxial static strain is regulated by protein kinase C α and focal adhesion kinase. *Circ. Res.* 94, 642–649.
- Maron, B.J., McKenna, W.J., 2003. *American College of Cardiology/European Society of Cardiology: clinical expert consensus document on hypertrophy cardiomyopathy*. *J. Am. College Cardiol.* 42, 1687–1713.
- McCrosan, Z.A., Billeter, R., White, E., 2004. Transmural changes in size, contractile and electrical properties of SHR left ventricular myocytes during compensated hypertrophy. *Cardiovasc. Res.* 63, 283–292.
- Menzel, A., 2005. Modelling of anisotropic growth in biological tissues—a new approach and computational aspects. *Biomech. Mod. Mechanobiol.* 3, 147–171.
- Naghdi, P., 1990. A critical review of the state of finite plasticity. *J. Appl. Math. Phys.* 41, 315–394.
- Omens, J.H., Vaplon, S.M., Fazeli, B., McCulloch, A.D., 1998. Left ventricular geometric remodeling and residual stress in the rat heart. *J. Biomech.* 31, 715–719.
- Opie, L.H., 2003. *Heart Physiology: From Cell to Circulation*. Lippincott Williams & Wilkins, Philadelphia.
- Parker, K.K., Tan, J., Chen, C.S., Tung, L., 2008. Myofibrillar architecture in engineered myocytes. *Circ. Res.* 103, 340–342.
- Rodriguez, E.K., Hoger, A., McCulloch, A.D., 1994. Stress-dependent finite growth in soft elastic tissues. *J. Biomech.* 27, 455–467.
- Rosamond, W., Flegal, K., Friday, G., Furie, K., Go, A., Greenlund, K., Haase, N., Ho, M., Howard, V., Kissela, B., Kittner, S., Lloyd-Jones, D., McDermott, M., Meigs, J., Moy, C., Nichol, G., Odonnell, C., Roger, V., Rumsfeld, J., Sorlie, P., Steinberger, J., Thom, T., Wasserthiel-Smoller, S., Hong, Y., 2007. Heart disease and stroke statistics-2007 update: a report from the American Heart Association Statistics Committee and Stroke Statistics Subcommittee. *Circulation* 115, 69–171.
- Sanger, J.W., Ayoob, J.C., Chowrashi, P., Zurawski, D., Sanger, J.M., 2000. Assembly of myofibrils in cardiac muscle cells. *Adv. Exp. Med. Biol.* 481, 89–102 (discussion 103–105).
- Sawada, K., Kawamura, K., 1991. Architecture of myocardial cells in human cardiac ventricles with concentric and eccentric hypertrophy as demonstrated by quantitative scanning electron microscopy. *Heart Vessels* 6, 129–142.
- Smith, S.H., Bishop, S.P., 1985. Regional myocyte size in compensated right ventricular hypertrophy in the ferret. *J. Mol. Cell Cardiol.* 17, 1005–1011.
- Taber, L.A., 1995. Biomechanics of growth, remodeling and morphogenesis. *Appl. Mech. Rev.* 48, 487–545.
- Taber, L.A., Humphrey, J.D., 2001. Stress-modulated growth, residual stress, and vascular heterogeneity. *J. Biomech. Eng.* 123, 528–535.
- Tracqui, P., Ohayon, J., Boudou, T., 2008. Theoretical analysis of the adaptive contractile behavior of a cardiomyocyte cultured on elastic substrates with varying stiffness. *J. Theor. Biol.* 225, 92–105.
- Verdier, C., Etienne, J., Duperray, A., Preziosi, L., 2009. Rheological properties of biological materials. *Comput. Rend. Phys.* 10, 790–811.
- Yoshida, M., Sho, E., Nanjo, H., Takahashi, M., Kobayashi, M., Kawamura, K., Honma, M., Komatsu, M., Sugita, A., Yamauchi, M., Hosoi, T., Ito, Y., Masuda, H., 2010. Weaving hypothesis of cardiomyocyte sarcomeres. *Am. J. Pathol.* 176, 660–678.
- Zohdi, T.I., Holzapfel, G.A., Berger, S.A., 2004. A phenomenological model for atherosclerotic plaque growth and rupture. *J. Theor. Biol.* 227, 437–443.